Original Article

Development of hybrid shielding system for large-area Compton camera: A Monte Carlo study

Jae Hyeon Kim [a], Junyoung Lee [a], Young-su Kim [b], Hyun Su Lee [a], Chan Hyeong Kim [a, *]

[a] Department of Nuclear Engineering, Hanyang University, 222 Wangsimni-ro, Seongdong-Gu, Seoul, 04763, South Korea
[b] National Radiation Emergency Medical Center, Korea Institute of Radiological & Medical Science, 75 Nowon-ro, Nowon-Gu, Seoul, 01812, South Korea

ARTICLE INFO

ABSTRACTS

Compton cameras using large scintillators have been developed for high imaging sensitivity. These scintillator-based Compton cameras, however, mainly due to relatively low energy resolution, suffer from undesired background-radiation signals, especially when radioactive materials' activity is very low or their location is far from the Compton camera. To alleviate this problem for a large-size Compton camera, in the present study, a hybrid-type shielding system was designed that combines an active shield with a veto detector and a passive shield that surrounds the active shield. Then, the performance of the hybrid shielding system was predicted, by Monte Carlo radiation transport simulation using Geant4, in terms of minimum detectable activity (MDA), signal-to-noise ratio (SNR), and image resolution. Our simulation results show that, for the most cases, the hybrid shielding system significantly improves the performance of the large-size Compton camera. For the cases investigated in the present study, the use of the shielding system decreased the MDA by about 1.4, 1.6, and 1.3 times, increased the SNR by 1.2−1.9, 1.1−1.7, and 1.3−2.1 times, and improved the image resolution (i.e., reduced the FWHM) by 7−8, 1−6, and 3−5% for ^{137}Cs, ^{60}Co, and ^{131}I point source located at 1−5 m from the imaging system, respectively.

1. Introduction

Compton imaging, which uses Compton kinematics-based electronic collimation to select effective events for imaging [1], is considered to be a very promising technology for imaging of the location or distribution of radioactive materials emitting gammas. Recently, Compton cameras that use large scintillators, such as the Large-area Compton Camera (LACC) [2] and the Dual Particle Imager (DPI) [3], have been developed to maximize imaging sensitivity. Especially, the LACC shows high performance for both imaging sensitivity and imaging resolution, due to the use of a large-area monolithic scintillator and an advanced position-estimation algorithm (i.e., MLPE, maximum-likelihood position estimation).

If the activity of the radioactive material is very low or the location of the radioactive material is very distant, however, Compton cameras using scintillators cannot image the location of the radioactive material, due mainly to the relatively low energy resolution of scintillator-based detectors. In such cases, the

performance of the Compton camera can be improved by properly shielding it from background radiation.

In the present study, a shielding system was designed for a large-size Compton camera, the LACC, by Monte Carlo radiation transport simulations with Geant4 (version 10.04.p02) [4]. The shielding system was designed as a hybrid system, which combines an active shield with a veto detector and a passive shield that surrounds the active shield. A simple model for the simulation of background radiation was also developed and tested. Then, the performance of the hybrid shielding system was evaluated in terms of changes in minimum detectable activity (MDA), signal-to-noise ratio (SNR), and image resolution.

2. Development of background radiation equivalent source (BRES) model

2.1. Selection of dominant gamma energies and measurement of photopeaks

For a gamma imaging device on the ground or in a regular room of a concrete building, the main component of the background radiation is terrestrial gammas. In order to simulate terrestrial
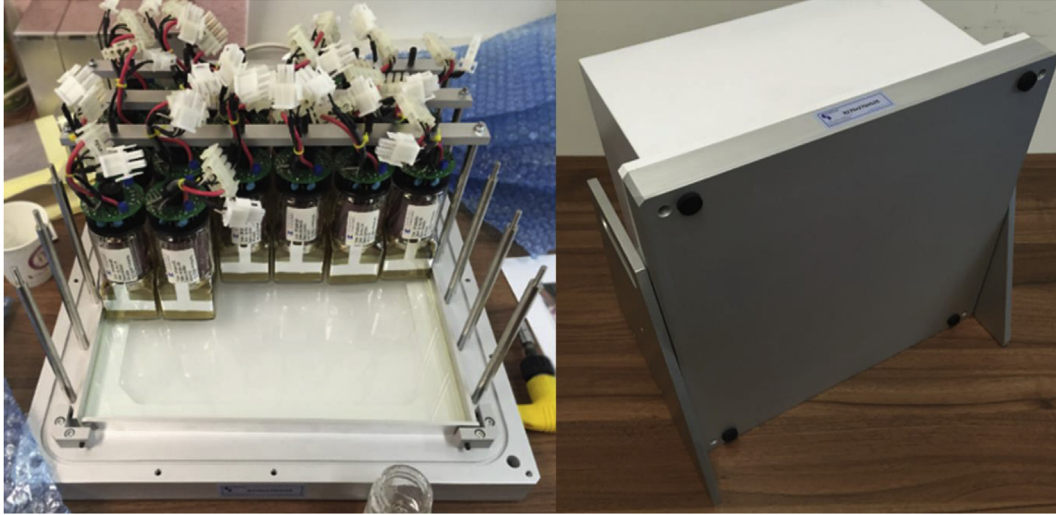
Fig. 1. 3-cm-thick NaI(Tl) monolithic scintillation detector.

gammas, in principle, the concentration and composition of radioactive nuclides should be measured for the surrounding materials (e.g., ground, wall), which process is complicated and very time-consuming. In the present study, therefore, we developed a simple model, called 'background radiation equivalent source (BRES),' which can provide the energy spectrum of the background radiation at a given location without measuring the concentration and composition of radioactive nuclides.

Note that most terrestrial gammas come from ^{238}U series, ^{232}Th series, and ^{40}K [5]. In the present study, we assumed that the background gammas can be expressed as a linear combination of these three sets of nuclides in the surrounding materials. We also assumed that the ^{238}U and ^{232}Th series are in secular equilibrium [6].

In order to determine the number of disintegrations of these three nuclide sets in the surrounding materials for a given level of background radiation, some major gammas were first selected for these three nuclide sets. For this, the most dominant (i.e., with highest emission yield) 609.31 and 1460.83 keV gammas were
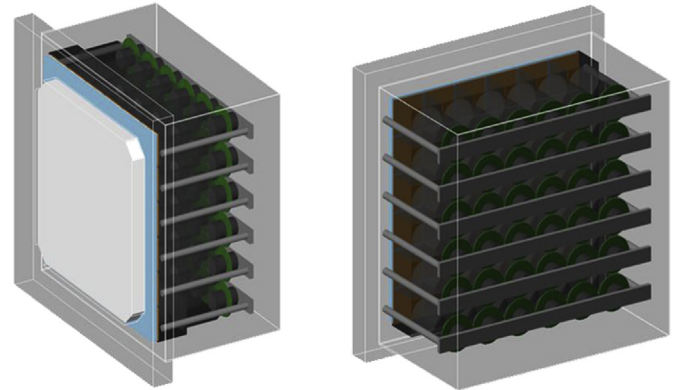

Fig. 3. Geant4 model of 3-cm-thick NaI(Tl) monolithic scintillation detector.

selected for the ^{238}U series and ^{40}K, respectively [6]. For the ^{232}Th series, however, the second dominant 2614.53-keV gamma was selected because the most dominant 236.63-keV gamma peak is
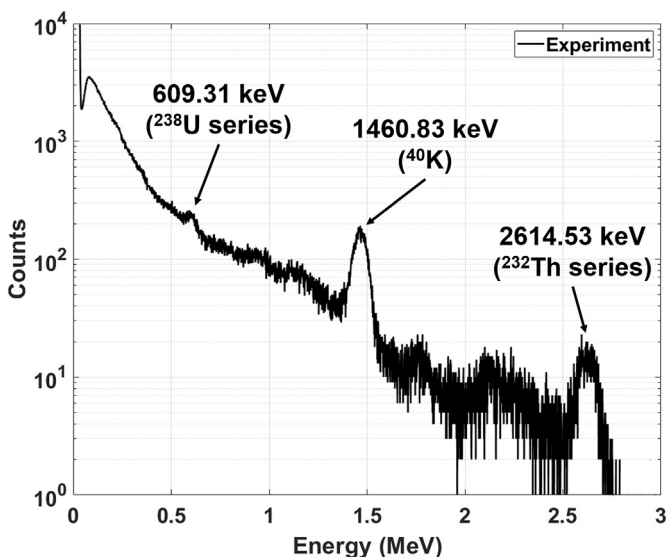

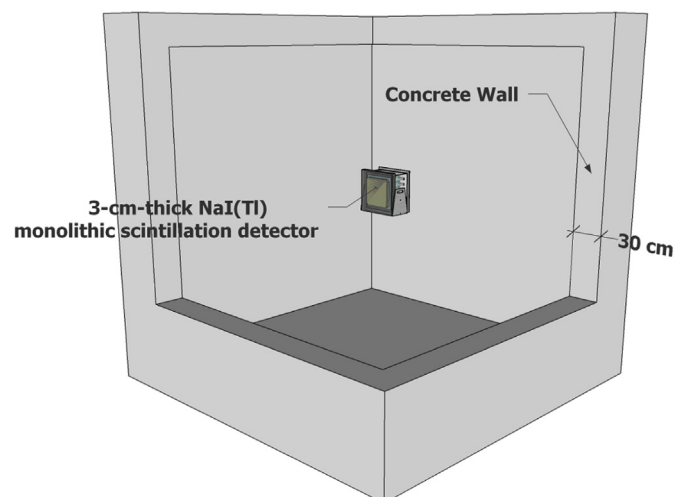Fig. 2. Measured energy spectrum for background radiation.

Fig. 4. 3-cm-thick NaI(Tl) monolithic scintillation detector and concrete wall as modeled in Geant4.
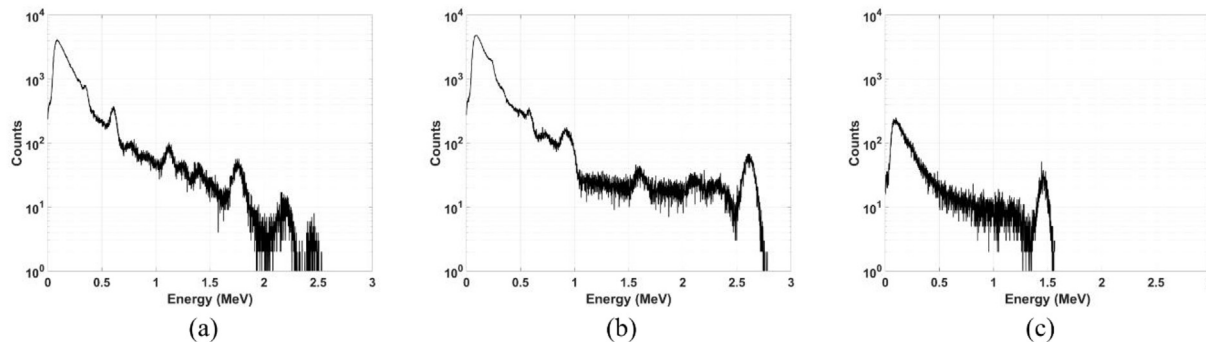
Fig. 5. Simulated energy spectra for ^{238}U series (a), ^{232}Th series (b), and ^{40}K (c).

difficult to distinguish from the backscattered peak on the Compton continuum of higher-energy gammas.

Next, the background radiation was measured for 5 min using a 3-cm-thick NaI(Tl) monolithic scintillation detector (Fig. 1) [7], which is a component detector of the LACC, in a regular room of a concrete building where the entire experiment was performed. Then, the peak areas for the selected major gamma peaks were calculated in the measured energy spectrum.

Note that the 3-cm-thick NaI(Tl) monolithic scintillation detector is composed of a planar monolithic NaI(Tl) scintillator and a closely packed array of 36 square-type photomultiplier tubes (PMTs). The dimension of the NaI(Tl) scintillator is 27 cm (W) × 27 cm (H) × 3 cm (T). This detector in the LACC is called an absorber detector. The LACC is composed of this absorber detector and a scatter detector that is identical to the absorber detector except that the thickness of the NaI(Tl) scintillator is 2 cm, not 3 cm.

Fig. 2 shows the measured energy spectrum in which the photopeaks of the selected gammas are all well identified. The peak areas for the selected major gamma peaks were 2,450, 1,118, and 11,488 counts for 609 ± 50 keV (^{238}U series), 2614 ± 104 keV (^{232}Th series), and 1460 ± 77 keV (^{40}K), respectively.

2.2. Determination of photopeak efficiencies for major gammas

The photopeak efficiencies of the 3-cm-thick NaI(Tl) monolithic scintillation detector for the major gammas were determined by
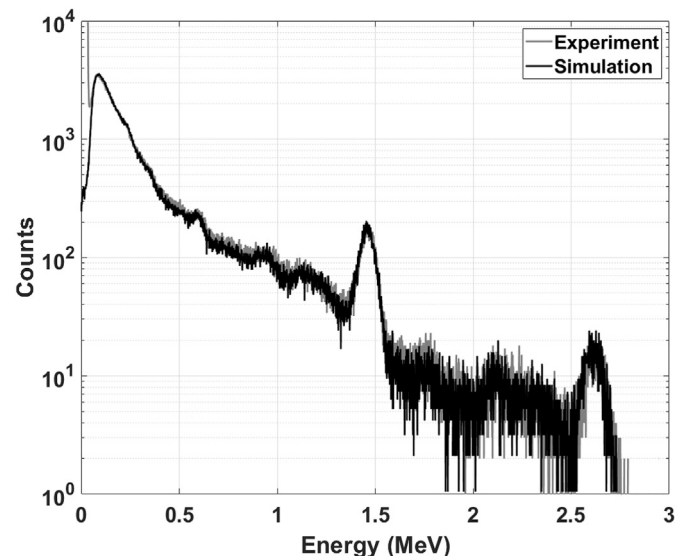
Monte Carlo radiation transport simulations with Geant4. First, simulations were performed separately to simulate the energy spectrum of the detector induced by each set of nuclides (^{238}U series, ^{232}Th series, and ^{40}K) distributed in the wall of the concrete room. The Geant4 model of the detector is shown in Fig. 3. The G4_CONCRETE (density = 2.3 g/cm^3) [8] in Geant4 was used as the material for the concrete wall, and the thickness of the wall was assumed to be 30 cm. The detector was assumed to be located in the center of the room (3 m × 3 m × 3 m), as shown in Fig. 4. G4EmLivermorePhysics was used for transporting photons and electrons. The energy deposited in the NaI(Tl) scintillator was calculated by simply summing deposited energy of every step inside the scintillation crystal volume which is recorded by GetTotalEnergyDeposit function of Geant4 library. For applying the experimental response of the detector accurately in the simulations, the energy resolution of the detector was reflected based on the empirical formula, which was determined by a separate
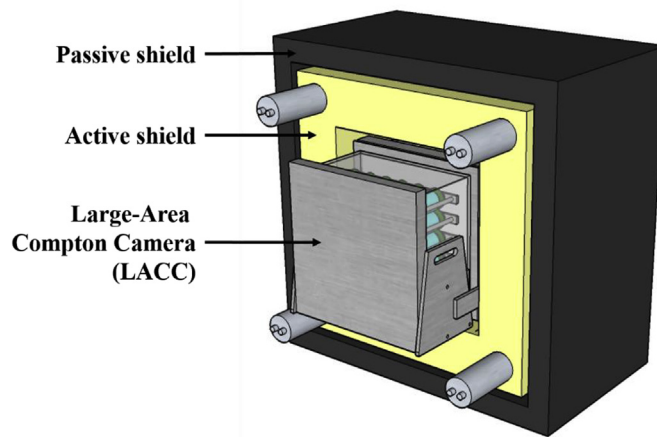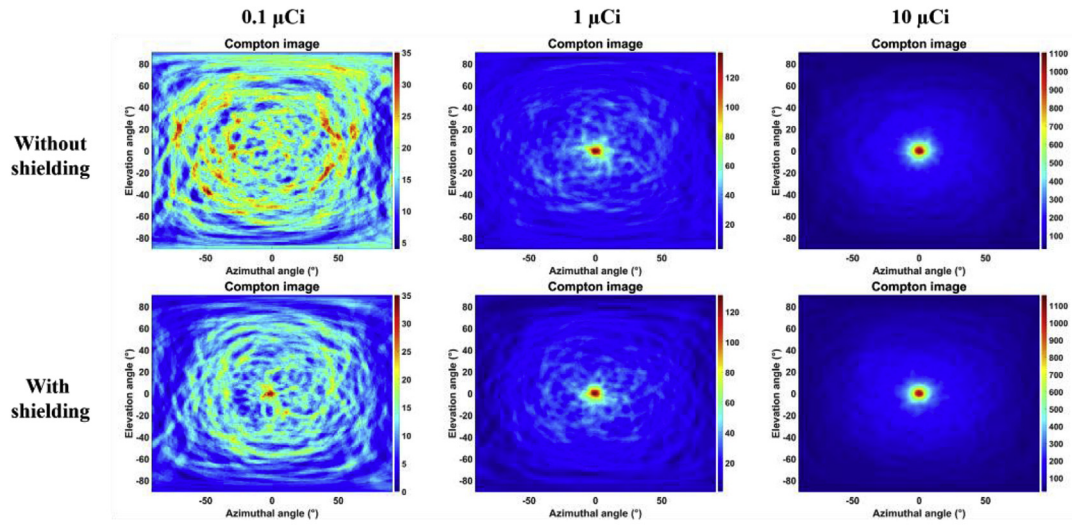

Fig. 7. Configuration of hybrid shielding system around LACC.

Table 1
Estimated MDA, SNR, and image resolution for 10-μCi ^{137}Cs point source.

Index	Distance	Without hybrid shield	With hybrid shield
MDA	1 m	0.156 ± 0.007 μCi	0.109 ± 0.006 μCi
	2 m	0.595 ± 0.029 μCi	0.412 ± 0.021 μCi
	5 m	3.68 ± 0.16 μCi	2.58 ± 0.14 μCi
SNR	1 m	11.7 ± 0.3	14.1 ± 1.5
	2 m	7.31 ± 0.33	11.3 ± 1.1
	5 m	2.49 ± 0.24	4.79 ± 0.42
Image resolution (FWHM)	1 m	12.7° ± 0.3°	11.8° ± 0.2°
	2 m	13.2° ± 0.6°	12.2° ± 0.4°
	5 m	16.1° ± 1.6°	14.9° ± 0.8°

Fig. 6. Simulated and measured energy spectra of background radiation for 3-cm-thick NaI(Tl) detector (= absorber detector).

Source distance - 1 m

Source distance - 2 m

Source distance - 5 m

Fig. 8. Simulated Compton images of ^{137}Cs point source for LACC without hybrid shielding system (upper) and with hybrid shielding system (lower). The images represent different distances (1, 2, and 5 m) and different source activities (0.1, 1.0, and 10 μCi).
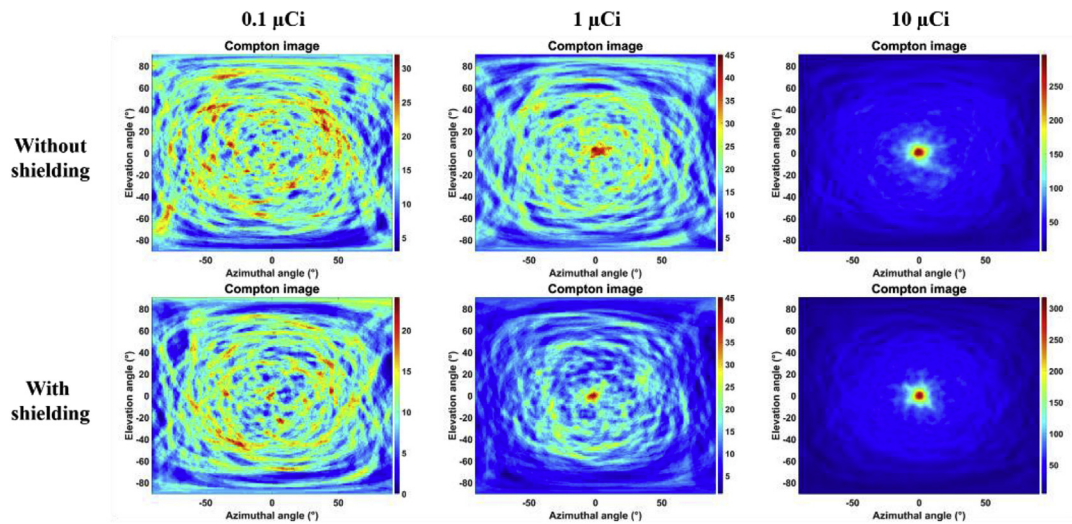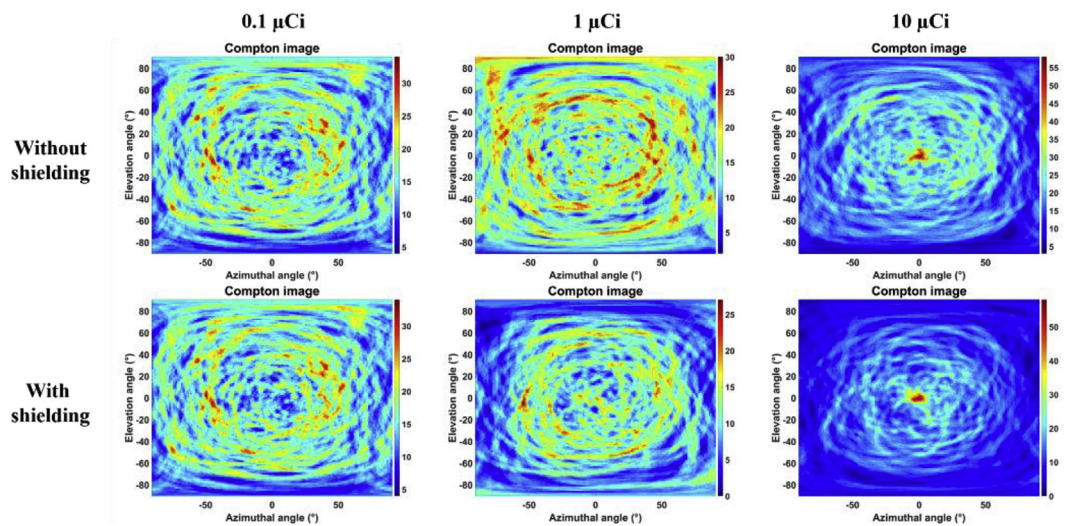
Table 2
Estimated MDA, SNR and image resolution for 10-μCi ^{60}Co point source.

Index	Distance	Without hybrid shield	With hybrid shield
MDA	1 m	0.097 ± 0.004 μCi	0.061 ± 0.003 μCi
	2 m	0.366 ± 0.014 μCi	0.227 ± 0.013 μCi
	5 m	2.25 ± 0.08 μCi	1.39 ± 0.07 μCi
SNR	1 m	25.0 ± 1.1	28.7 ± 0.9
	2 m	14.4 ± 0.8	21.4 ± 1.1
	5 m	4.01 ± 0.39	7.00 ± 0.53
Image resolution (FWHM)	1 m	9.58° ± 0.4°	9.44° ± 0.3°
	2 m	10.2° ± 0.5°	9.77° ± 0.4°
	5 m	13.5° ± 0.8°	12.8° ± 0.7°

measurement using check sources [7]. The radioactive nuclides were assumed to be uniformly distributed in the concrete wall, and 10^9 disintegrations were simulated for each of the nuclide sets; that is, the gamma-rays were emitted homogeneously and isotropically in all concrete volume following simulated energy spectra. Fig. 5 shows the simulated energy spectra for the ^{238}U series, ^{232}Th series, and ^{40}K. By applying the same energy window as in the experiments, the photopeak efficiencies for the 609.31, 2614.53, and 1460.83 keV gammas were determined to be 2.25 × 10^{-6}, 5.67 × 10^{-6}, and 1.91 × 10^{-6} s^{-1}Bq^{-1}, respectively.

2.3. Construction of BRES model

For each of the selected major gammas, the number of disintegrations in the concrete wall that would produce the same size of photopeak in the energy spectrum of the five-minute measurement was calculated by dividing the photopeak counts (from the measurement) by the photopeak efficiency (from the simulation). The numbers of disintegrations were calculated as 1.09 × 10^9, 1.97 × 10^9, and 6.01 × 10^9 for the ^{238}U series, ^{232}Th series, and ^{40}K, respectively. The BRES model was finally defined as the sum of the three nuclide sets distributed in the concrete wall with the aforementioned numbers of disintegrations. That is, in subsequent Monte Carlo simulations, the background radiation field was simulated as the radiation field produced from the ^{238}U series, ^{232}Th series, and ^{40}K radioisotopes, which are homogeneously distributed in the concrete wall (see Fig. 4) with the aforementioned numbers of disintegrations, i.e., 1.09 × 10^9, 1.97 × 10^9, and 6.01 × 10^9, respectively.

Fig. 6 compares the simulated energy spectrum generated from the developed BRES model and the measured energy spectrum, which shows that the generated energy spectrum is very close to the measured one, not only for the selected major gamma peaks of 609.31 keV, 2614.53 keV, and 1460.83 keV, but also for the nearly entire energy range, even below 250 keV. There is a large difference below 30 keV, which was due to the fact that the electronic noises were not modeled in the present study. Note that the energy less than 30 keV is not very important in Compton imaging, which does not show good performance for low-energy gammas. The entire process was repeated for the 2-cm-thick NaI(Tl) monolithic scintillation detector (i.e., scatter detector), and similar results were obtained.

3. Design and performance prediction of hybrid shielding system

3.1. Configuration of hybrid shielding system

Using the developed background model, a hybrid shielding system was developed for the LACC [2]. The configuration of the hybrid shielding system for the LACC is shown in Fig. 7. The hybrid shielding system surrounds all faces of the 3-cm-thick NaI(Tl) monolithic scintillation detector (i.e., the absorber detector) of the LACC, except for the surface facing the 2-cm-thick NaI(Tl) monolithic scintillation detector (i.e., the scatter detector). The main feature of the hybrid shielding system is the use of both passive shielding and active shielding. The passive shield, which is the outer layer of the hybrid shielding system, physically blocks the background radiation, mainly terrestrial gammas, from entering the LACC, while the active shield, which is the inner layer of the hybrid shielding system, acts as a veto detector wired to the component detectors of the LACC with an anticoincidence logic.

The purpose of the passive shield is to physically block radiation that comes from the side and back of the LACC. Note that when we image ^{137}Cs (662 keV) and ^{60}Co (1173 keV and 1332 keV), which are of major interest for Compton imaging in the nuclear industry and the nuclear decommissioning, the 1.46-MeV gammas from ^{40}K are the main obstacle, due to their energy and intensity. In the present study, the passive shield was designed to a 6-cm thickness of iron in order to reduce the intensity of the 1.46-MeV gammas by ~90%.

The active shield (= plastic scintillation detector) discriminates the background gammas serving as a veto detector. That is, it is expected that the active shield filters out the events in which an incoming background gamma is scattered in the plastic scintillation detector, and then has an additional interaction in one or more of the component detectors. The active shield also filters out 'false' effective events in which the incident photons from the front side of the LACC (i.e., from the radioactive material/source of interest) are scattered in the scatter detector and then also scattered in the absorber detector, and in which case too, the sum energy of the scatter and absorber detector happens to fall within the range of the sum energy window of the LACC for a given radiation source. These false effective events are treated as effective events in regular Compton cameras without an active shield. The active shield is composed of a 15-cm-thick plastic scintillator and four 3-inch cylindrical PMTs coupled to the scintillator.

The outer dimension of the hybrid shielding system is 92 cm (W) × 92 cm (H) × 48 cm (T) with a hollow well of 50 cm (W) × 50 cm (H) × 27 cm (T) that fits the absorber detector of the LACC. The weight of the LACC and the hybrid shielding system are 75 kg and 1283 kg, respectively.

### 3.2. MDA, SNR, and image resolution

The performances of the hybrid shielding system were evaluated in terms of the change in minimum detectable activity (MDA), signal-to-noise ratio (SNR), and image resolution. Each term was estimated as follows:

(a) MDA, which is the minimum source activity that can be imaged using the LACC, was calculated using the equation [5]:

Source distance - 1 m
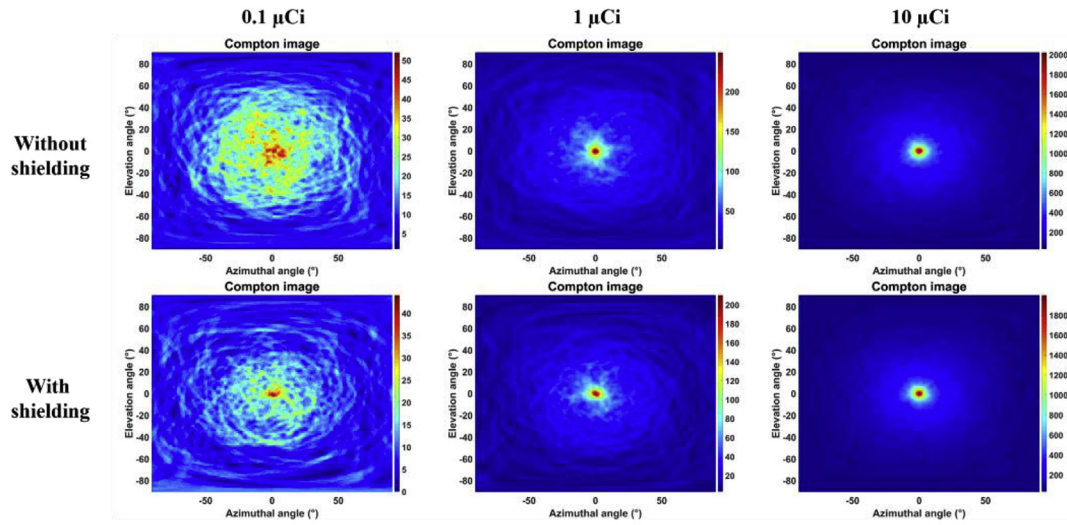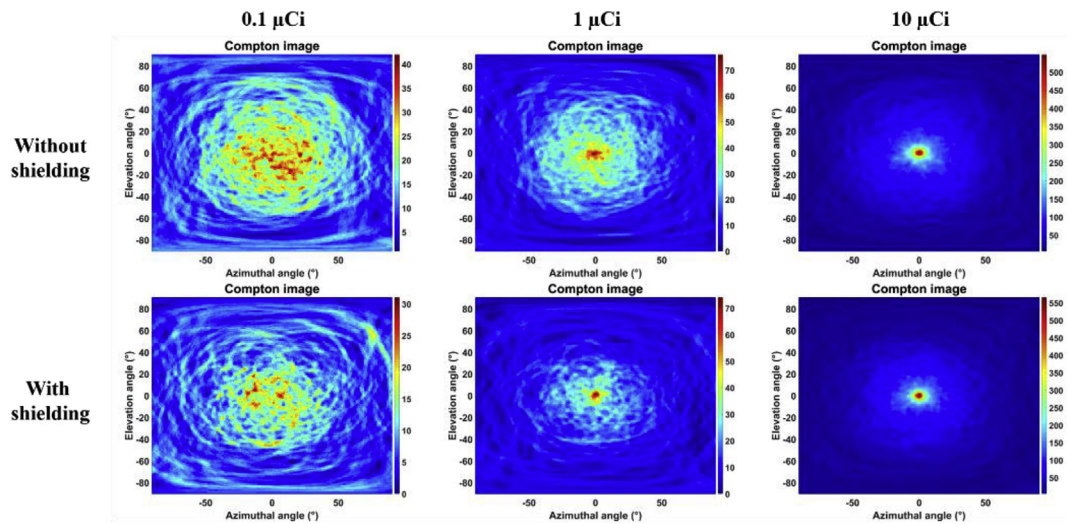
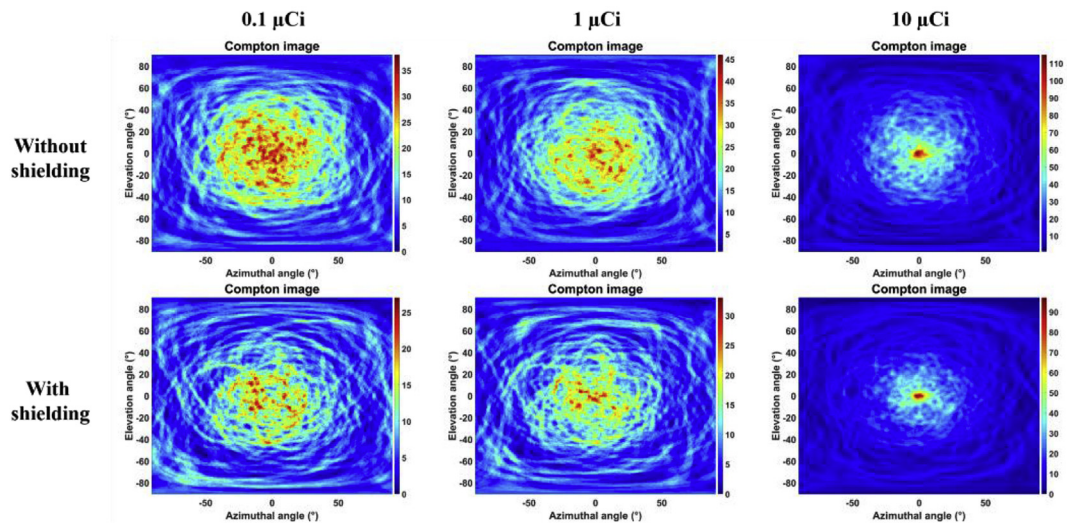**Source distance - 2 m**

Source distance - 5 m

Fig. 9. Simulated Compton images of ⁶⁰Co point source for LACC without hybrid shielding system (upper) and with hybrid shielding system (lower). The images represent different distances (1, 2, and 5 m) and different source activities (0.1, 1.0, and 10 μCi).

$$MDA = \frac{N_D}{\varepsilon TY} \tag{1}$$

where N_D is the minimum number of counts needed for detection, ε is the absolute detection efficiency of the LACC, T is the measurement time, and Y is the emission yield of the major gamma. The N_D was calculated as follows:

$$L_C = N_{cf} + 1.645\sqrt{N_{cf}} \tag{2}$$

$$N_D = L_C + 1.645\sqrt{N_D} \tag{3}$$

where L_C is the critical level, and N_{cf} is the background cone fluctuation. The N_{cf} was calculated using the standard deviation of the index value for the background gammas in the Compton image.

(b) SNR was calculated as follows [9]:

$$SNR = \frac{m_{T,max} - \overline{m}_B}{\sigma_{m_B}} \tag{4}$$

where $m_{T,max}$ is the maximum index value for the source in the Compton image, $\overline{m}_B$ is the average index value of the background, and σ_{m_B} is the standard deviation of the index value of the background in the Compton image.

(c) Image resolution was evaluated in terms of the full width at half maximum (FWHM) averaged for the horizontal and vertical directions.

The performance of the hybrid shielding system was evaluated for 27 different cases by Geant4 Monte Carlo simulations. The simulations were performed for a point source of three nuclides: ^{137}Cs and ^{60}Co, which are of major interest in the nuclear industry and ^{131}I, which represents radioactive material emitting low-energy gammas. For each nuclide, a total of 9 simulations were performed, i.e., by changing the activity of the source and the distance of the source from the camera. The considered activities and distances were 0.1 μCi, 1.0 μCi, and 10.0 μCi and 1 m, 2 m, and 5 m, respectively. The imaging time was assumed to be 3 min in all cases. The energy windows of 662 ± 60, 1250 ± 150, and 364 ± 40 keV were applied to select the gammas of interest for ^{137}Cs, ^{60}Co, and ^{131}I, respectively.

3.3. Results of performance prediction

Table 1 shows the values of MDA, SNR, and image resolution (FWHM) as estimated from the simulations of the 10.0-μCi ^{137}Cs source. The MDA values of the LACC for the ^{137}Cs point-source were 0.156 μCi, 0.595 μCi, and 3.68 μCi for the 1, 2, and 5 m source

distances, respectively. The use of the hybrid shielding system reduced the MDA by ~1.4 times for all of the source distances; that is, the MDA values were reduced to 0.109 μCi, 0.412 μCi, and 2.58 μCi.

The table also shows that the use of the hybrid shielding system improves the SNR by 1.2−1.9 times, with the improvement increasing with the source distance. Note that if the source activity is very large or the source is very close to the imaging system, the effect of the background gammas will be very limited, and therefore, the use of the hybrid shielding system will not be very effective; on the other hand, if the source activity is very low or the source is very far from the imaging system, the effect of the background gammas will be large and the image could be dominated by background gammas, in which case, the use of the hybrid shielding system will be effective.

The use of the hybrid shielding system also improved image resolution (i.e., reducing FWHM) by 7−8% for all of the source distances, which is to say, from 12.7°, 13.2°, and 16.1° FWHM to 11.8°, 12.2°, and 14.9° FWHM for 1, 2, and 5 m, respectively.

Fig. 8 presents the Compton images simulated for the ^{137}Cs point source with and without applying the hybrid shielding system for the same three source distances (1, 2, and 5 m) and three source activities (0.1, 1.0, and 10.0 μCi). The results generally show that the use of the hybrid shielding system significantly improves image quality, except for the images of very high statistics. Especially, for the 0.1-μCi point source at 1 m, the LACC without the hybrid shielding system was not able to provide the location of the source, whereas the LACC with the hybrid shielding system was able to determine the real location of the same source. This result roughly agrees with the calculated MDAs for the LACC without the hybrid shielding system (= 0.156 μCi) and with the hybrid shielding system (= 0.109 μCi) for the 1 m source distance in Table 1.

Table 2 and Fig. 9 show the results for the ^{60}Co point source. The use of the hybrid shielding system reduced the MDA by ~1.6 times for all of the distances and also improved the SNR by 1.1−1.7 times, following the same trend of increasing improvement with source distance. The use of the hybrid shielding system improved the SNR, but the improvement was smaller compared with that in the ^{137}Cs case, due seemingly to the facts that higher-energy gammas with higher yields (i.e., 1170 keV gamma 100% and 1330 keV gamma 100%) are emitted from ^{60}Co and that the effect of the background gammas on the LACC is therefore smaller for a given source activity and source distance. The use of the hybrid shielding system improved the image resolution by 1−6% considering all of the source distances.

Table 3 and Fig. 10 show the results for the ^{131}I point source. The use of the hybrid shielding system reduced the MDA by ~1.3 times for all of the source distances. The use of the hybrid shielding system significantly improved the SNR, specifically by 1.3−2.1 times, following the same trend of increasing improvement with source distance. This significant SNR improvement seems due to
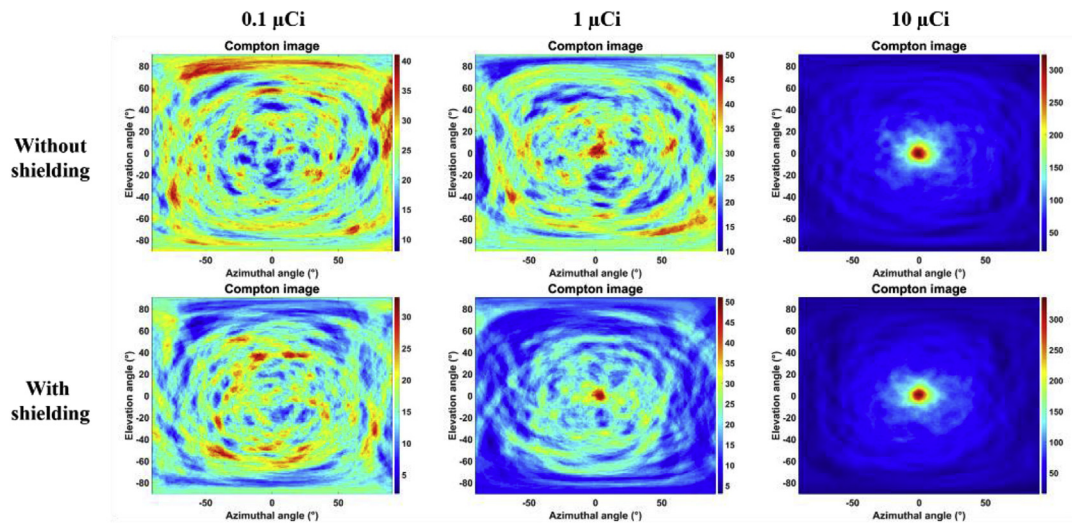
Table 3
Estimated MDA, SNR and image resolution for 10-μCi ^{131}I point source.

Index	Distance	Without hybrid shield	With hybrid shield
MDA	1 m	0.163 ± 0.009 μCi	0.125 ± 0.006 μCi
	2 m	0.626 ± 0.031 μCi	0.481 ± 0.028 μCi
	5 m	3.93 ± 0.21 μCi	3.02 ± 0.18 μCi
SNR	1 m	9.16 ± 0.44	12.1 ± 0.7
	2 m	5.59 ± 0.28	7.49 ± 0.37
	5 m	1.54 ± 0.18	3.18 ± 0.29
Image resolution (FWHM)	1 m	19.7° ± 0.8°	18.7° ± 0.6°
	2 m	20.0° ± 0.7°	19.3° ± 0.6°
	5 m	22.1° ± 0.9°	21.1° ± 0.8°

Source distance - 1 m
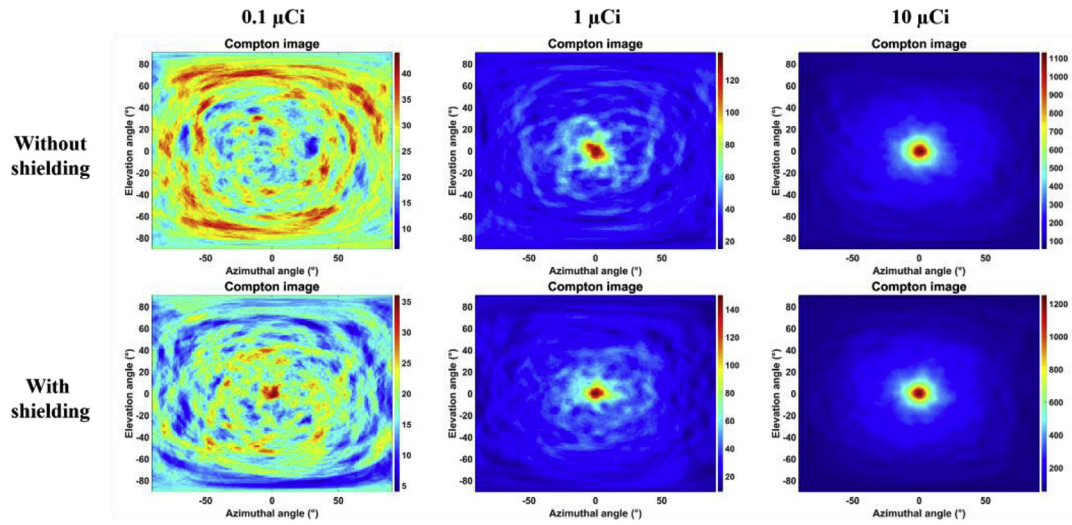
Source distance - 2 m
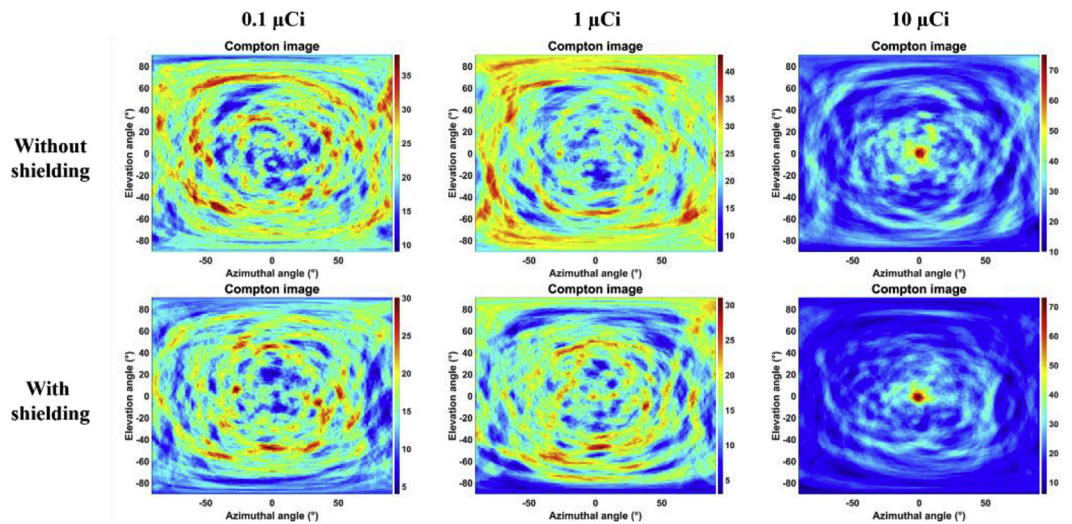

Source distance - 5 m

Fig. 10. Simulated Compton images of ^{131}I point source for LACC without hybrid shielding system (upper) and with hybrid shielding system (lower). The images represent different distances (1, 2, and 5 m) and different source activities (0.1, 1.0, and 10 μCi).

the facts that the lower-energy gammas with lower yields (i.e., 81% yield for 364 keV gamma) are emitted from ^{131}I and, therefore, that the effect of the background gammas on the LACC is relatively larger when compared to ^{137}Cs and ^{60}Co for a given source activity and source distance. The use of the hybrid shielding system improved the image resolution by 3–5% considering all of the source distances.

4. Conclusion

In the present study, a hybrid-type shielding system was designed for a large-size Compton camera, which combines an active shield with a veto detector and a passive shield that surrounds the active shield. Then, the performance of the hybrid shielding system was estimated by Monte Carlo radiation transport simulation using Geant4. For this, first, a background-source model for terrestrial background gammas was developed based on a measured energy spectrum. Then, using the developed background-source model, the performance of the hybrid shielding system for the LACC was predicted by Monte Carlo simulations. The results generally showed that, for the most cases, the use of the hybrid shielding system significantly improves the imaging performance of the LACC. For the cases investigated in the present study, the use of the shielding system decreased the MDA by 1.4, 1.6, and 1.3 times, increased the SNR by 1.2–1.9, 1.1–1.7, and 1.3–2.1 times, and improved the image resolution (i.e., reduced the FWHM) by 7–8, 1–6, and 3–5% for the ^{137}Cs, ^{60}Co, and ^{131}I point sources, respectively, that were located 1–5 m from the imaging system.

Declaration of competing interest

The authors declare that they have no known competing financial interests or personal relationships that could have appeared to influence the work reported in this paper.

Acknowledgement

References

[1] R.W. Todd, J.M. Nightingale, D.B. Everett, A proposed gamma camera, Nature 251 (1974) 132–134.

[2] Y. Kim, J.H. Kim, J. Lee, C.H. Kim, Large-area Compton camera for high-speed and three-dimensional imaging, IEEE Trans. Nucl. Sci. 65 (2018) 2817–2822.

[3] A. Poitrasson-Rivière, M.C. Hamel, J.K. Polack, M. Flaska, S.D. Clarke, S.A. Pozzi, Dual-particle imaging system based on simultaneous detection of photon and neutron collision events, Nucl. Instrum. Methods Phys. Res. Sect. A Accel. Spectrom. Detect. Assoc. Equip. 760 (2014) 40–45.

[4] S. Agostinelli, J. Allison, K. Amako, J. Apostolakis, H. Araujo, P. Arce, M. Asai, D. Axen, S. Banerjee, G. Barrand, F. Behner, L. Bellagamba, J. Boudreau, L. Broglia, A. Brunengo, H. Burkhardt, S. Chauvie, J. Chuma, R. Chytracek, G. Cooperman, G. Cosmo, P. Degtyarenko, A. Dell'Acqua, G. Depaola, D. Dietrich, R. Enami, A. Feliciello, C. Ferguson, H. Fesefeldt, G. Folger, F. Foppiano, A. Forti, S. Garelli, S. Giani, R. Giannitrapani, D. Gibin, J.J. Gomez Cadenas, I. Gonzalez, G. Gracia Abril, G. Greeniaus, W. Greiner, V. Grichine, A. Grossheim, S. Guatelli, P. Gumplinger, R. Hamatsu, K. Hashimoto, H. Hasui, A. Heikkinen, A. Howard, V. Ivanchenko, A. Johnson, F.W. Jones, J. Kallenbach, N. Kanaya, M. Kawabata, Y. Kawabata, M. Kawaguti, S. Kelner, P. Kent, A. Kimura, T. Kodama, R. Kokoulin, M. Kossov, H. Kurashige, E. Lamanna, T. Lampen, V. Lara, V. Lefebure, F. Lei, M. Liendl, W. Lockman, F. Longo, S. Magni, M. Maire, E. Medernach, K. Minamimoto, P. Mora de Freitas, Y. Morita, K. Murakami, M. Nagamatu, R. Nartallo, P. Nieminen, T. Nishimura, K. Ohtsubo, M. Okamura, S. O'Neale, Y. Oohata, K. Paech, J. Perl, A. Pfeiffer, M.G. Pia, F. Ranjard, A. Rybin, S. Sadilov, E. di Salvo, G. Santin, T. Sasaki, N. Savvas, Y. Sawada, S. Scherer, S. Sei, V. Sirotenko, D. Smith, N. Starkov, H. Stoecker, J. Sulkimo, M. Takahata, S. Tanaka, E. Tcherniaev, E. Safai Tehrani, M. Tropeano, P. Truscott, H. Uno, L. Urban, P. Urban, M. Verderi, A. Walkden, W. Wander, H. Weber, J.P. Wellisch, T. Wenaus, D.C. Williams, D. Wright, T. Yamada, H. Yoshida, D. Zschiesche, GEANT4 - a simulation toolkit, Nucl. Instrum. Methods Phys. Res. Sect. A Accel. Spectrom. Detect. Assoc. Equip. 506 (2003) 250–303, https://doi.org/10.1016/S0168-9002(03)01368-8.

[5] A. Poitrasson-Rivière, B.A. Maestas, M.C. Hamel, S.D. Clarke, M. Flaska, S.A. Pozzi, G. Pausch, C.-M. Herbach, A. Gueorguiev, M.F. Ohmes, J. Stein, Monte Carlo investigation of a high-efficiency, two-plane Compton camera for long-range localization of radioactive materials, Prog. Nucl. Energy 81 (2015) 127–133, https://doi.org/10.1016/j.pnucene.2015.01.009.

[6] S. Li, L. Wang, Y. Cheng, X. Tuo, M. Liu, F. Yao, F. Leng, Y. Cheng, T. Cai, Y. Zhou, A novel natural environment background model for Monte Carlo simulation and its application in the simulation of anticoincidence measurement, Appl. Radiat. Isot. 108 (2016) 75–81, https://doi.org/10.1016/j.apradiso.2015.12.036.

[7] Y.-S. Kim, J.H. Kim, H.S. Lee, C.H. Kim, Position-sensitive NaI(TL) detector module for large-area Compton camera, J. Kor. Phys. Soc. 72 (2018), https://doi.org/10.3938/jkps.72.26.

[8] NIST listings, Compositions of materials used in STAR databases. http://physics.nist.gov/cgi-bin/Star/compos.pl?matno=144.

[9] A. Del Guerra, N. Belcari, W. Bencivelli, A. Motta, S. Righi, A. Vaiano, G. Di Domenico, E. Moretti, N. Sabba, G. Zavattini, R. Campanini, N. Lanconelli, A. Riccardi, M.N. Cinti, R. Pani, R. Pellegrini, Monte Carlo study and experimental measurements of breast tumor detectability with the YAP-PEM prototype, in: 2002 IEEE Nuclear Science Symposium Conference Record vol. 3, 2002, pp. 1887–1891, https://doi.org/10.1109/nssmic.2002.1239691. Norfolk, VA, USA, Nov 10–16.